Composites Communications 65 (2026) 102850

Contents lists available at ScienceDirect

Composites Communications

journal homepage: www.elsevier.com/locate/coco

Research article

A high-throughput method to determine the electrical percolation threshold of conductive polymer nanocomposite inks via gradient direct ink writing

Stijn De Smedt [a], Quanrun Dong [a,b], Francisco Molina-Lopez [c], Ruth Cardinaels [a,b,*]

[a] Soft Matter, Rheology and Technology (SMaRT), Chemical Engineering Department KU Leuven, Celestijnenlaan 200J, 3001, Heverlee, Vlaams-Brabant, Belgium
[b] Processing and Performance of Materials, Mechanical Engineering Department TU Eindhoven, P.O. Box 513, 5600 MB, Eindhoven, Noord-Brabant, The Netherlands
[c] Surface and Interface Engineered Materials, Materials Engineering Department KU Leuven, Kasteelpark Arenberg 44, 3001, Heverlee, Vlaams-Brabant, Belgium

ARTICLE INFO

Keywords:
Electrical percolation threshold
Direct ink writing
Gradient printing
Rheology
Conductive polymer nanocomposites

ABSTRACT

This study presents a high-throughput method for determining the electrical percolation threshold (EPT) of conductive polymer nanocomposite inks using gradient direct ink writing (DIW) printing. Traditional methods require the preparation of numerous discrete samples to determine the EPT. To address this limitation, the authors modified a commercial FDM printer to feature a continuous mixing DIW setup capable of extruding inks with a graded filler concentration. The method was validated using a plasticized starch matrix loaded with carbon black (CB). Filler concentration was determined via thermogravimetric analysis (TGA). By correlating electrical resistance measurements with local filler concentration along a single printed gradient strand, the EPT was successfully identified at 2.7 wt%. This approach offers a significant reduction in material consumption and characterization time compared to conventional sample-by-sample testing.

1. Introduction

With the electrification of numerous applications in daily life and the shift to renewable and sustainable energy sources, the demand for lightweight, biobased and flexible electronics is increasing at a fast pace [1]. Conductive polymer composites (CPCs) are a promising class of materials to meet demands in applications like stretchable wearables [2], environmentally friendly supercapacitors [3], antistatic fibers [4] and flexible electromagnetic interference shields [5,6] as they combine the processability and flexibility of polymers with the electrical properties of conductive fillers [7]. They consist of an insulating polymer matrix in which conductive fillers are dispersed. When the filler content exceeds a critical concentration, the electrical percolation threshold (EPT), a continuous network of conductive pathways is formed throughout the composite. This leads to a drastic increase in the electrical conductivity of the material, often over several orders of magnitude for a relatively small increase in filler content [1,4].

The EPT itself is influenced by various factors, including the type, shape, and size of the filler particles [8–10], the interaction with and type of polymer matrix [11], the dispersion within the matrix [6,12], the crystallinity or morphology of the matrix [13,14], the combined presence of other particles that can affect the distribution and exfoliation [15,16] and the processing method used to fabricate the composite, which affects filler distribution and dispersion and possibly introduces filler alignment [17–20]. Understanding and controlling the EPT is crucial in optimizing the electrical properties of CPCs for specific applications, such as flexible electronics, sensors, and electromagnetic interference shielding [6]. Knowing the exact percolation threshold allows for the design of composites with tailored electrical properties while minimizing the amount of conductive filler used, which can be more cost-effective. Traditional methods for determining the percolation threshold involve preparing a series of composite samples with different filler concentrations and measuring their electrical conductivity [4]. Besides using experimental methods, electrical percolation can also be predicted via different modeling approaches, whereby phenomena like electron tunneling, electron hopping, dielectric relaxation and interfacial polarization need to be taken into account [21–23].

A traditional approach to determine the EPT of carbon black (CB) in different polymer matrices was followed by Choi et al. [4], who used melt extrusion to prepare 11 different loadings of CB in three different polymers: polypropylene (PP), polyethylene terephthalate (PET) and Nylon. They measured the electrical conductivity of compression molded films of each composition by the 4-point probe method and determined a percolation region as a range of loadings where a significant increase in conductivity was observed. The percolation thresholds of their films were found to be 1–3 wt% for PP and PET, where the electrical conductivity increased by 6 to 7 orders of magnitude and

* Corresponding author.
E-mail addresses: Ruth.Cardinaels@kuleuven.be, R.M.Cardinaels@tue.nl (R. Cardinaels).

https://doi.org/10.1016/j.coco.2026.102850
Received 4 March 2026; Received in revised form 14 May 2026; Accepted 16 May 2026
Available online 22 May 2026
2452-2139/© 2026 The Authors. Published by Elsevier Ltd. This is an open access article under the CC BY license (http://creativecommons.org/licenses/by/4.0/).

3–5 wt% for Nylon where an increase of 4 orders of magnitude was recorded. This study also underlines the influence of the polymer matrix on the percolation threshold. The polarity of the amide groups in Nylon likely led to a poorer dispersion of the CB particles compared to the non-polar PP and PET matrices, resulting in a higher EPT. Similarly, Azizi et al. [24] produced low-density polyethylene (LDPE) disks with CB via batch extrusion with recirculation and compression molding and reported an EPT of 20 wt%. They measured the electrical response via a dielectric spectrometer. Moreover, Moacy et al. [25] reported an EPT of 10 wt% for CB loaded high-density polyethylene (HDPE) produced in a similar manner.

Also biobased polymer matrices have been used to produce CPCs with CB as a conductive filler, with the added advantage of being biodegradable. This type of composites have gained interest in the fields of biobased composite electronics, smart sensors and flexible supercapacitors [26] due to their biodegradability, processability and low cost. Ma et al. [27] produced glycerol plasticized-starch membranes and observed a different EPT for samples produced via different dispersion methods. Peidayesh et al. [28] produced starch-based composites with different loadings of CB. Prior to the processing, they sonicated the suspensions of CB in glycerol and water to obtain a good dispersion. They reported an increase in conductivity of three orders of magnitude between 5.5 wt% and 8 wt% of CB loading and report the percolation threshold of their material as 5.5 wt%. Comparing the EPTs of these relatively analogous systems, it obviously shows that a large span of reported values is present in literature. The processing and characterization of the material are definitely key aspects in the reported electrical behavior of the produced material.

Additive manufacturing of graded materials has gained significant attention in recent years due to its potential to create complex structures with tailored properties [29,30]. Besides the application potential of functionally graded materials, spatially varying material properties on a 2D map, by varying composition, temperature, chemistry, laser intensity, printing conditions, etc. [31,32] can be used as a combinatorial and high throughput measurement technique for studying material properties [31]. Direct ink writing (DIW) is a particularly promising technique for fabricating graded materials, as it allows for precise control over the composition and structure of the printed object by varying the ink formulation or printing parameters during the manufacturing process. Recently, several works have reported on DIW of gradient materials for various applications. Often, gradients are obtained with a single nozzle DIW setup and a single ink by varying the printing parameters, leading to differences in geometry and porosity across layers [33,34]. Alternatively, a commercial mixing head, namely the ViscoDuo-VM03 (Viscotec, Germany), which is a two-component dosing system, was used to continuously mix two clay-based inks with different compositions before extrusion. By varying the ratio of both inks during printing, Tang et al. [35] created a gradient in composition in the printed object. Simultaneously, they varied the infill density layer by layer to create a second gradient in porosity. They demonstrated the potential of this method by printing geological models with varying mechanical properties and permeability. Combination with other techniques like thermal spraying provides additional tunability and the possibility to enhance anisotropic performance [36].

Such gradients are especially relevant in the field of biomedical engineering. To replicate physiological structures, biofabrication strategies must move beyond simple layer-by-layer stacking towards methods that allow continuous transitions and precise spatial control [37]. To realize such gradients in printed bodies, the field is moving towards the integration of microfluidics into extrusion printheads enabling amongst others core–shell extrusion [38,39], multilayer extrusion [40,41] and continuous mixing of bioinks [42]. The use of microfluidic printheads is possible in this field due to the generally lower viscosities of the used bioinks compared to polymer nanocomposite DIW inks. The challenge in this regard is to obtain a setup that can handle the higher viscosities while still allowing for precise control over the mixing and extrusion process of multimaterial DIW inks.

As the applications in which CPCs are used increase in complexity, it becomes more important to precisely define the EPT. Additive manufacturing allows for the fabrication of CPCs with controlled filler distributions and gradients in concentration [29,30]. However, there is no clear determination method for the EPT of such printed materials yet. To this end, we propose a method based on DIW of a conductive graded strand and thermogravimetric analysis (TGA) to determine the EPT. Hereby we use the spatial mapping of the conductivity via gradient direct ink writing as a high-throughput characterization method. We demonstrate this method on a plasticized starch-based conductive composite ink loaded with carbon black (CB). The method involves the synthesis of two inks, one of pure plasticized starch and one with a CB loading well above the EPT. These materials are subjected to rheological characterization to assess their printability. Contrary to the use of a commercial system, which is complex and expensive, a commercial FDM printer is equipped for DIW with an in-house designed and produced continuous mixing setup, allowing the flow rate control of two highly viscous inks, to print single samples with a gradient in concentration. The printed samples are then characterized optically and electrically to determine the EPT based on the local composition and conductivity. This approach allows for a more efficient and detailed investigation of the electrical percolation in CPCs, providing optimization of these materials for applications where precise tuning of the percolated network is key. Simultaneously, this work demonstrates the development of a low-cost multimaterial DIW printer capable of printing gradients in composition. Finally, the combination of numerical simulations and local concentration measurements allows to analyze the achieved gradient concentration profiles.

2. Modifying a commercial FDM printer for gradient DIW

An Ender 3 Pro (Creality, China) FDM 3D printer is modified to allow for direct ink writing (DIW) using 5 ml syringes. Originally, this is a small single extruder filament printer which is upgraded and modified into a DIW printer able to combine two distinct material streams in a continuous way. The printer has been equipped with a second Z-axis for stability. The hotend, extruder and tubing have been removed and are replaced by a custom made geometry which allows for continuous mixing during printing as shown on the left in Fig. 1a. To implement this on the printer, the required modifications include switching the motherboard to one which can drive two extruder motors separately, designing and producing the add-ons and modifying the printer's firmware. The original motherboard is replaced by a BTT SKR E3 Turbo (BigTreeTech, China) which can drive two independent extruder motors. The printer firmware is modified from standard Marlin firmware to RepRapFirmware (RRF) to enable the G-code commands to control both extruder motors separately. To make all of this possible and practical on the printer, the power supply is repositioned to the back of the device and a new RRF compatible screen has been installed on the front. The printer can read G-code-files from a micro-SD card or can be controlled via USB-serial connection and a computer running the RepetierHost software.

The produced X-gantry allows for continuous mixing of two inks in a static mixer before extrusion. A design based on a plunger screw is used to push the ink from the 5 ml syringe into a mixing nozzle. The final design is based on printing methods reported in literature, but adapted to fit the Ender 3 printer [43,44]. Instead of using an external syringe pump, we designed an integrated system where the syringe plunger is directly driven by the stepper motor. By using a plunger screw inside the syringe directly, the torque of the motor can be directly transferred to the material in the syringe without lead screw, which benefits the extrusion accuracy and consequently the quality of the printed object. The plunger screws are driven by NEMA 17 stepper motors and the syringes are held in place by a custom made insert which is mounted on

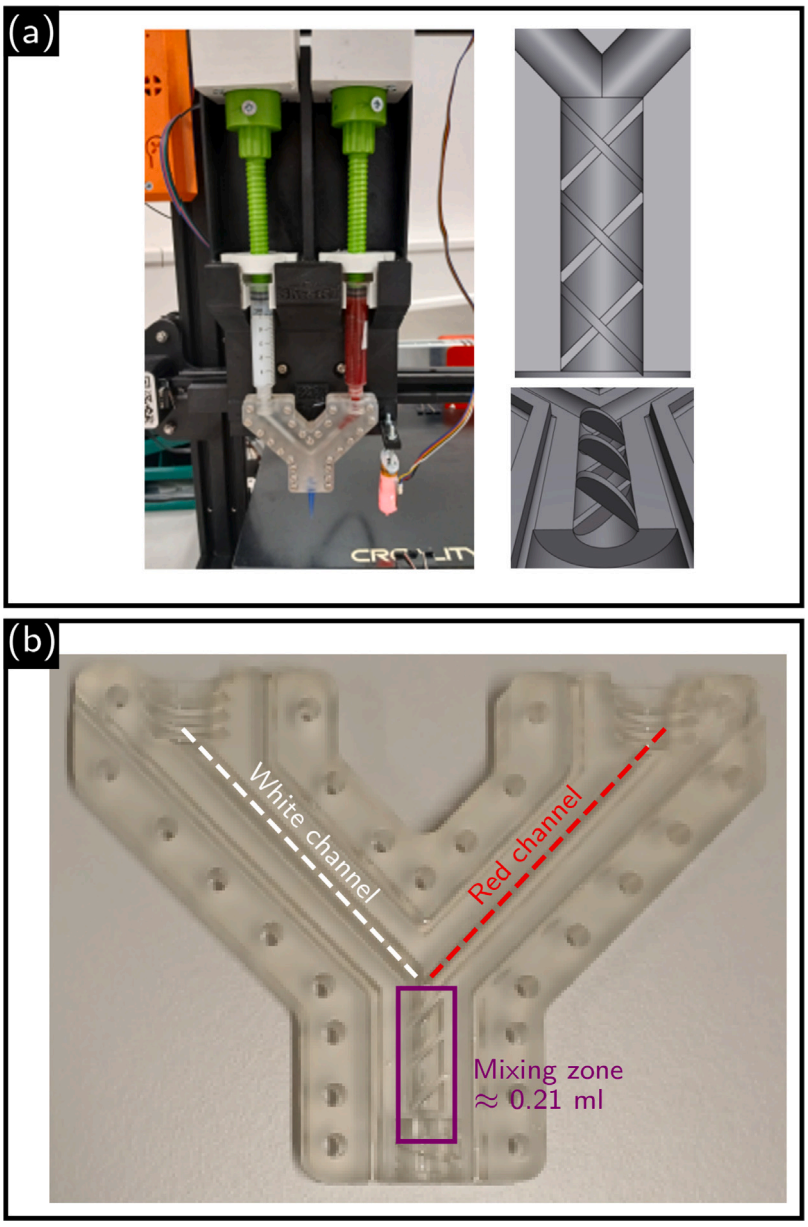

Fig. 1. (a) Picture of the continuous mixing setup mounted on the modified Ender 3 Pro DIW printer (left) and top view (top right) as well as side view (bottom right) of the static mixer model inside the mixing channel. (b) Detailed picture of the static mixer nozzle. The inlet channels for both syringes and the outlet channel with mixing elements are indicated.

the X-gantry. A screwthread is present in the insert and on the plunger screw, so when the motor turns, the plunger screw moves downwards or upwards depending on the direction of rotation. The syringes are directly connected to the mixing nozzle via luer locks. All pieces, the gantry, the plungers, the inserts, the connection pieces and the mixing nozzle are designed and fabricated in house.

The mixing nozzle itself consists of two halves which can be screwed tight together and can be further sealed with glue if necessary. In each halve, a Y-shaped channel is present which goes from the inlets to the outlet where a tapered tip can be screwed in as printing nozzle. Inside the outlet channel, baffles are present such that when both halves are screwed together, an inline static mixer with elliptical blades and three mixing elements is formed [45]. The principle of the mixer is sketched on the right in Fig. 1a. Fig. 1b shows one halve of the mixing nozzle and indicates the inlet channels in white and red and the mixing element in the outlet channel. The mixing nozzle is 3D printed using a Formlabs Form 3 (Formlabs, USA) printer with a layer height of 50 μm. A gauge 14 tapered tip, with an inner diameter of 1.6 mm is connected to the outlet of the nozzle to print the materials. When filling both syringes with different inks, this two-in-one-out setup allows for continuous mixing of the inks by controlling the amount of extrusion of each syringe independently. This way, a gradient in composition can be obtained in the printed object. The theoretical dead volume of the mixing channel is calculated to be 0.21 ml, based on the dimensions of the mixing channel and the excluded volume of the mixing elements. This means that when switching from one pure ink to the other, a theoretical volume of at least 0.21 ml needs to be extruded before the new composition is reached at the outlet. Technical drawings of all parts can be found in **Figures S.1–S.4** in the SI.

3. Materials and methods

3.1. Formulation of plasticized starch based composite inks

Starch from wheat, glycerol, sorbitol and citric acid (Sigma-Aldrich, USA) are used as the base materials for the DIW ink. As a conductive filler, Printex XE2 extra-conductive carbon black (CB) (Degussa, Germany), with a particle size of 30–40 nm is used. All products are used as received without further purification or preprocessing. The plasticized starch matrix is prepared by mixing starch, glycerol, sorbitol and citric acid in a weight ratio of 100:30:30:40. Water is added to the mixture in excess and it is stirred by hand to ensure dissolution of all components prior to the plasticization step. The mixture is then heated to 80 °C under continuous magnetic stirring to plasticize the starch. First, the viscosity will increase due to gelatinization of the starch granules, after which the viscosity will decrease again as the granules rupture and the starch chains solubilize. This marks the end of the plasticization process [46]. The plasticized starch solution is held at this elevated temperature to evaporate the excess water and obtain a viscous ink suitable for DIW. When the desired volume, such that the final water content is 50 wt%, is reached, the ink is cooled down to room temperature and stored airtight to prevent drying. Before storage, the obtained ink can be split into two batches, one of which is colored with allura red dye (Sigma-Aldrich, USA) to visualize the transition zone during printing.

To prepare the composite inks, the starch is plasticized as described above but without the glycerol in the mixture. The desired amount of conductive filler is added to a 250:1 (w/w) water/glycerol solution in which the amount of glycerol corresponds to the final content in the ink [27]. The filler is dispersed in this aqueous glycerol solution using a UP400S ultrasonic probe mixer (Hielscher, Germany) with a maximal power output of 400 W. Dispersion occurs in three intervals of increasing intensity. First the suspension is sonicated for 30 min at 300 W and a cycle of 0.8. The second step consists of sonication at 320 W for 30 min and a cycle of 0.9. Finally, the last dispersion interval uses 340 W for 10 min continuously. Afterwards, the dispersion is added to the plasticized starch mixture at 80 °C and the mixture is magnetically stirred to ensure homogeneity. Finally, the evaporation of excess water takes place to yield a viscous ink suitable for DIW.

The inks are loaded into 5 ml syringes for DIW additive manufacturing, that are then connected to the mixing nozzle. Before printing, the channels in the mixing nozzle are filled such that the ink which should be extruded first is present at the outlet and the other ink reaches the junction point. Step function prints as well as fast and slow gradients are performed with dyed plasticized starch inks to ensure the correct functioning of the setup and to determine the transition zone going from one ink to the other. Afterwards, fast gradient prints are executed to create a CB concentration graded strand between the two inks. The printed samples are left to dry overnight before characterization.

3.2. Rheology of plasticized starch based composite inks

An MCR501 stress-controlled rheometer (Anton Paar, Austria) is used to characterize the rheological properties of the inks and assess their printability, based on previous work [47]. The measurements are performed with a 25 mm parallel plate geometry at a temperature of 25 °C. Mineral oil is placed around the sample to avoid the evaporation of water. The rheological characterization of the inks includes frequency sweeps, strain amplitude sweeps, flow rate sweeps and three interval thixotropy tests. The strain amplitude sweep at 10 rad s^{-1} is performed from 0.1 to 100% strain to determine the linear viscoelastic region (LVR) of the inks. In this work, the end of the LVR is defined as the strain at which the storage modulus G' drops below 10% of its plateau value. The frequency sweep is executed with a strain amplitude well in the linear regime. The frequency is varied from 100 to 0.1 rad s^{-1} to determine the storage modulus G' and loss modulus G'' of the inks. The flow rate sweep is performed by increasing the shear rate from 0.01 to 100 s^{-1} and recording the viscosity. This test is also immediately performed from 100 to 0.01 s^{-1} on the same sample. The shear rates are logarithmically spaced in time to obtain 5 points per decade and the time per shear rate is determined by the instrument's software (Rheoplus, version 3.11). One rate sweep takes approximately 10 min. Finally, a classic three interval thixotropy test is performed to assess the recovery behavior of the inks after shear. First, a low shear rate of 0.5 s^{-1} is applied for 120 s, followed by a high shear rate of 50 s^{-1} for 120 s to simulate the shear during extrusion. Finally, the low shear rate is applied again for 240 s to monitor the recovery of the ink structure. The viscosity is recorded throughout the test. Each test is performed in triplicate on freshly loaded samples from the same batch of ink.

3.3. DIW of a gradient dye/filler concentration

Two G-code protocols are written to characterize the mixing setup and to determine the EPT of the composite. When the step function print is executed, the printer prints a strand in the form of a snake-like sample, going back and forth over a length of 120 mm and spacing each line 5 mm apart. The first few lines are printed with only extrusion from the first syringe, after which the extrusion is switched to the second syringe only. The transition zone going from the first to the second material is characterized by analyzing the color change in the printed sample when one of the inks is colored with a dye. The second G-code, the gradient print, is used to print a similar snake-like sample, but now the extrusion gradually changes from the first syringe to the second syringe over the course of printing by controlling the relative extrusion rates of both syringes and keeping the total extrusion volume per length constant at 0.004 ml cm^{-1}, at a printing speed of 250 mm min^{-1}. The fast gradient is programmed such that the total change should be obtained in 25 times going back and forth. After each time printing back and forth, the extrusion ratio changes with 1/25 of the total change. The slow gradient print is programmed to obtain half the color change over the same course of printing and with the same printing parameters. The printing of one entire graded sample takes approximately 1.5 ml of ink.

3.4. Characterization of the printed concentration profiles

The composition profile along the printed sample is characterized in an optical and a thermogravimetric way for the colored and the conductive composite ink respectively. The optical characterization relies on the gradual color change in the printed sample when the step function or a gradient function is printed, starting with uncolored and transitioning to colored ink. The color is analyzed along the printed sample and is a measure for the transition zone introduced by the static mixer in the mixing nozzle. Pictures of the printed strands are taken using an iPhone 13 and image analysis using the Fiji Colorinspector (ImageJ2, Open Source) is conducted to determine the color change along the printed strands and quantify the transition from white to red extruded material. The color difference between colors along the sample and the end color of the strand are calculated using ΔE^*_{Lab}. In this method, each color is represented in the Lab coordinate system where L^* indicates the lightness of the color, a^* the green–red axis and b^* the yellow–blue axis [48]. The Lab coordinates of the first extruded pieces of material are determined in ImageJ as (L^*_2, a^*_2, b^*_2) and Eq. (1) is used with the Lab coordinates (L^*_1, a^*_1, b^*_1) at different segments of the printed sample to determine the difference with the initial color. A datapoint is taken every 120 mm along the printed strand:

$$\Delta E^*_{Lab} = \sqrt{(L^*_2 - L^*_1)^2 + (a^*_2 - a^*_1)^2 + (b^*_2 - b^*_1)^2}. \quad (1)$$

The color difference is scaled between 0 and 1, where 0 indicates the start of the printed sample and 1 the end of the printed sample. This way, the transition zone can be quantified and compared to the theoretical transition based on the dead volume of the mixing nozzle.

3.5. Determination of the electrical percolation threshold

The electrical resistance of different segments of the gradient sample from the pure matrix to a high filler content is measured to determine the percolation threshold of the composite system. A Fluke 287 true RMS multimeter (Fluke, USA) is used to measure the resistance of different segments along the printed sample using a current of 1 mA. The maximal resistance which can be measured with this device is 500 MΩ. The conductivity is calculated based on the measured resistance, the estimated cross-sectional area of the printed strand and the distance between the needle tipped probes, measured by means of a millimeter grid placed underneath the glass plate:

$$\sigma = \frac{L_r}{R \cdot A}, \tag{2}$$

where σ is the electrical conductivity [S m^{-1}], L_r is the distance between the voltage probes [m], R is the measured resistance [Ω] and A is the cross-sectional area of the printed sample [m^2]. The cross-sectional area is estimated by measuring the width and height of the printed sample with a digital caliper at different locations and taking the average value.

Thermogravimetric analysis (TGA) is performed on samples taken at different segments of the printed graded sample with a TGA Q500 (TA Instruments, USA). The samples are heated from 25 °C to 550 °C at 50 °C min^{-1} under N_2 and held isothermally for 1 h. The CB in each sample does not degrade under these thermal conditions. The residue at different points along the printed graded sample is determined as the residue after 60 min total experiment time when a plateau is reached. As a baseline, the mean residue of three samples of the pure plasticized starch matrix, which render an open loop measurement on the multimeter, is determined to account for any residue originating from the matrix itself (see **Figure S.5**). The local concentration of CB x_{CB} at different segments of the graded sample, is then obtained based on the measured sample residue r_{sample} and the determined residue of the pure plasticized starch matrix r_{matrix}:

$$x_{CB}\ [\text{wt\%}] = \frac{r_{sample} - r_{matrix}}{100 - r_{matrix}} \cdot 100. \tag{3}$$

The EPT is finally determined by plotting the conductivity as a function of the local CB concentration and fitting the data with a Boltzmann-sigmoidal curve [49,50]:

$$\sigma(x) = A_1 + \frac{A_2 - A_1}{1 + e^{[-A_3(x - A_4)]}}, \tag{4}$$

where $\sigma(x)$ is the electrical conductivity [S m^{-1}] and $[A_1, A_2, A_3, A_4]$ are the fitting parameters. A_1 and A_2 represent the minimum and maximum conductivity [S m^{-1}] respectively, A_3 is a parameter related to the slope of the curve at the inflection point [wt%$^{-1}$], A_4 is the concentration at the inflection point, representing the EPT [wt%] and x is the filler concentration [wt%]. While power-law scaling is frequently applied to the regime above percolation, the Boltzmann sigmoidal fit was utilized here to capture the diffuse nature of the transition and to provide a mathematically robust determination of the inflection point. As compared to the generalized effective medium (GEM) model, which we used in [13], the explicit equation of the Boltzmann sigmoidal fit makes it more practical than the GEM model. The curve_fit function from the SciPy library in Python is used to perform the fitting via non-linear least squares [51].

3.6. Simulation of the mixing process

To more quantitatively investigate the mixing process, numerical simulations were conducted to complement the experiments. The simulations were performed using COMSOL Multiphysics 6.4, coupling the Laminar Flow and Transport of Diluted Species interfaces through the velocity field. Herein, the conservation of mass, momentum and the advection–diffusion equations are solved. Time-dependent simulations were performed to capture the transient evolution of the flow and scalar fields during the extrusion process.

The geometry corresponds to the fluidic mixer connected to two inlet branches and one outlet channel, as shown in Fig. 1b. The computational domain represents the volume of the internal fluid of the mixer with inlet and outlet channels. The computational domain was discretized using an automatically generated unstructured mesh composed of triangular elements on surfaces and tetrahedral elements in the volume. Details of the mesh can be found in **Figures S.6** and **S.7** in the SI. A mesh independence study was conducted to ensure that the numerical results were insensitive to further mesh refinement. All simulations were performed in three dimensions. A segregated solver was used to handle the coupling between the fluid flow and concentration fields.

Both inlets were prescribed with mass flow boundary conditions, corresponding to syringe-driven injection. The total flow rate for each case was kept constant at 0.2 ml min^{-1}, corresponding to the experimental conditions. Three injection protocols were investigated, consistent with the experimental conditions. In the first protocol, the extrusion was suddenly switched from the left inlet to the right inlet. In the second and third protocol the flow rate from the left inlet linearly decreased from 0.2 to 0 ml min^{-1}, while simultaneously, the flow rate from the right inlet linearly increased from 0 to 0.2 ml min^{-1}, over a timespan of either 750 s or 1500 s, corresponding to the experimental conditions for respectively the fast and slow gradient. To compare with the experimental data, the time was shifted to account for the time needed for the red dye to fully fill the right arm of the mixer.

All channel walls were treated as no-slip boundaries. A scalar concentration of dye was prescribed at the inlets to distinguish the two fluid streams, with, for all cases, $c_d = 0$ mol m^{-3} at the left inlet and $c_d = 1$ mol m^{-3} at the right inlet. The fluid was modeled as a shear thinning non-Newtonian fluid. The density was set to $\rho = 1000$ kg m^{-3} and a power law viscosity model was employed based on the rheological measurements:

$$\eta = K\,\dot{\gamma}^{\,n-1}, \tag{5}$$

where K is the consistency index and n is the flow behavior index. Fitting of the experimental rheological data (**Figure S.8**) of the ink yielded $K = 77$ Pa s^n and $n = 0.27$, indicating pronounced shear thinning behavior. A constant diffusion coefficient of $D = 1 \times 10^{-9}$ m^2 s^{-1} was used for the dye, representative of molecular diffusion in liquids [52]. At the characteristic flow velocities and length scales of the mixer, diffusion is slow compared to advection, such that the scalar transport is predominantly convection-dominated. Since the dye is passive, it does not alter the rheological or hydrodynamic properties of the fluid.

4. Results and discussion

This section presents the results of the rheological characterization of the plasticized starch-based composite inks, their printability and the determination of the percolation threshold based on the printed concentration graded strands. The results of the simulations of the mixing nozzle are also discussed to provide further insight into the mixing behavior of the two inks in the static mixer.

4.1. Rheological characterization and printability of plasticized starch-based composite inks

The plasticized starch and composite inks are first rheologically characterized to investigate their suitability for DIW printing. Fig. 2 shows the results of the frequency sweeps on both materials. The average storage and loss moduli are visualized over the whole tested frequency range. Both inks show a predominantly elastic behavior over the full 0.1 to 100 rad s^{-1} frequency range as the storage modulus G' is higher than the loss modulus G''. The composite ink shows a higher storage modulus compared to the pure plasticized starch ink,

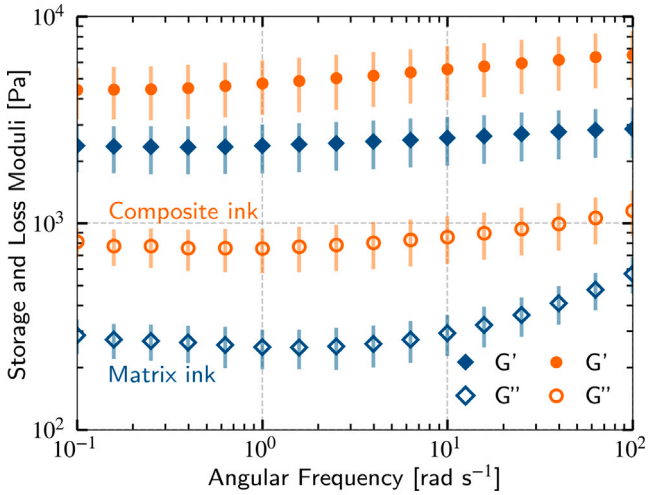

Fig. 2. Frequency sweeps on plasticized starch and composite inks showing the storage and loss moduli as a function of angular frequency, strain within the linear region. The error bars give the standard deviation on the repeat measurements.

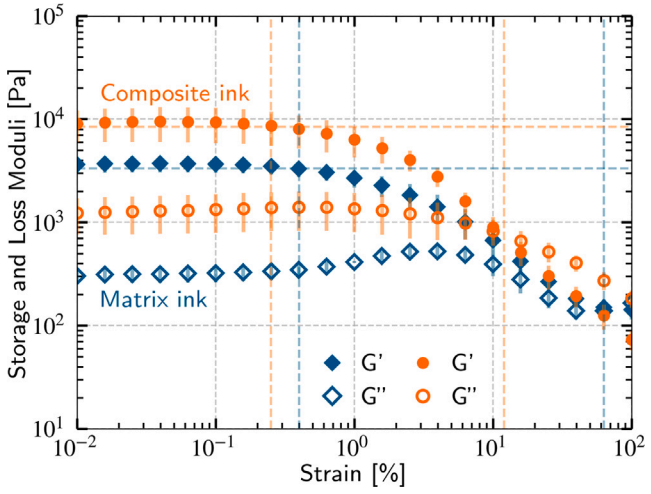

Fig. 3. Strain amplitude sweeps on plasticized starch and composite inks showing the storage and loss moduli as a function of strain amplitude at 10 rad s^{-1}. The orange and blue horizontal dashed lines indicate 90% of the plateau storage moduli. The orange and blue vertical dashed lines indicate the end of the linear viscoelastic region and the crossover points of both moduli at low and high strains respectively. The error bars give the standard deviation on the repeat measurements.

indicating a stiffer material due to the presence of the CB filler. The frequency dependence of both moduli is relatively weak, suggesting a stable network structure within the inks, which is favorable for shape retention after printing.

The results of strain amplitude sweeps are shown in Fig. 3. Both inks exhibit a linear viscoelastic region (LVER) up to a certain strain, beyond which the storage modulus G' decreases. The plateau storage modulus in the LVER has been determined as the average values at low strains (up to 0.1%) and is 3683 Pa and 9341 Pa for the matrix and the composite ink respectively. The end of the LVER, defined as the strain at which G' drops below 10% of its plateau value, is found to be 0.4% and 0.25% for the plasticized starch and composite ink respectively, as indicated on the figure. A first estimate of the yield stress for both materials is made by determining the stress at the crossover point of both moduli, which is often denoted as the flow stress [47]. This results in a yield stress of 129 ± 20 Pa and 122 ± 30 Pa for the plasticized starch and composite ink respectively, which are very similar. Moreover, the maximum in elastic stress for the composite material, another characteristic often used to quantify a yield stress [47], is 110 ± 20 Pa, which is very similar to the flow stress. For the matrix material, no maximum in the elastic stress is observed. In terms of yielding, there is no significant additional reinforcing effect of the carbon black filler in the system, which indicates that both materials can be expected to be similar to print.

Rotational rate sweeps are performed from 0.1^{-1} to 100 s^{-1} and back to 0.1 s^{-1} to investigate both inks under flow. The results are shown in Fig. 4 with viscosity datapoints corresponding to the left y-axis and shear stress data to the right y-axis. Both inks exhibit shear thinning behavior, as can be seen from the decrease in viscosity with increasing shear rate. This is a desirable property for DIW inks, as it allows for easy extrusion through the nozzle. The viscosity of both materials is similar at all tested shear rates, indicating that the addition of CB does not significantly alter the flow behavior of the plasticized starch matrix. This viscosity matching of both fluids is optimal for mixing, whereas high viscosity mismatches negatively influence the mixing efficiency due to the fact that the stress continuity at the interface causes the flow velocity of the low viscous stream to increase relative to that of the high viscous one [53]. The slope of the viscosity curve is around −1 for the composite ink, indicating yield stress dominated behavior. When looking at the shear stress, the dynamic yield stress σ_y^d can be estimated as the stress at the lowest shear rate for the downward rate sweep. For the pure plasticized starch ink, the

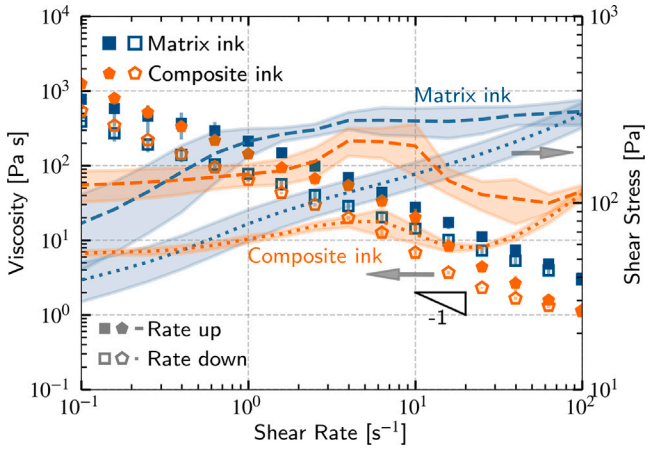

Fig. 4. Shear rate sweeps on plasticized starch and composite inks showing the viscosity (left y-axis) and shear stress (right y-axis) as a function of shear rate for increasing and decreasing shear rates. The error bars give the standard deviation on the repeat measurements for the viscosity. The shaded area indicates the standard deviation on the shear stress measurements.

slope is slightly less than −1 and no plateau in the shear stress is observed. Taking the stress at the lowest shear rate as the dynamic yield stress, this is 26.4 ± 8 Pa for this pure plasticized starch ink. For the composite ink, a plateau is present at low shear rates and the stress value at the plateau is 53.9 ± 3 Pa. It is obvious that the composite ink has a significantly higher dynamic yield stress compared to the pure matrix ink, which is expected due to the presence of the filler particles hindering flow. Comparing these yield stress values to the ones obtained from the oscillatory strain sweep, they are of the same order of magnitude for the composite ink but not for the pure plasticized starch ink. This can be due to the different measurement methods or the larger uncertainty on the dynamic yield stress in the rotational tests of the matrix ink. Overall, both inks show suitable rheological properties for DIW printing, with shear thinning behavior and a yield stress that can help maintain the shape of the printed object after extrusion [47].

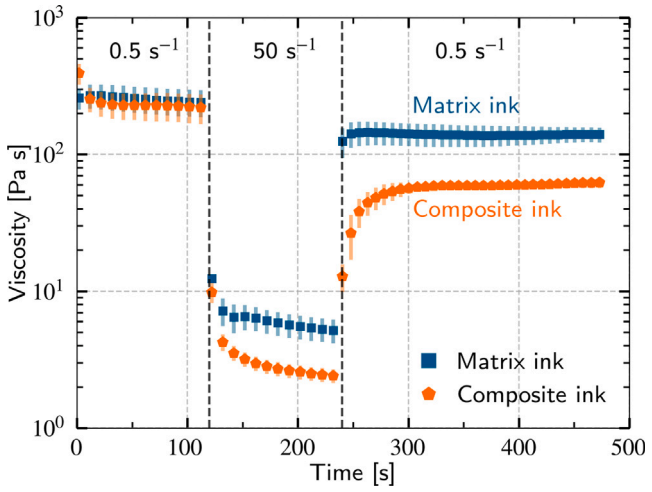

Fig. 5. Thixotropy tests on plasticized starch and composite inks showing the viscosity as a function of time under different shear rates. The error bars give the standard deviation on the repeat measurements.

The results of the thixotropy tests are shown in Fig. 5. Both inks show a significant drop in viscosity when the high shear rate is applied, simulating the extrusion process. Upon returning to the low shear rate, both inks exhibit a recovery in viscosity, indicating the rebuilding of an internal structure. The plasticized starch ink recovers to approximately 60% of its initial viscosity within the 240 s recovery period, while the composite ink recovers to about 30%. This suggests that both inks have acceptable structural recovery properties after shear, which is beneficial for maintaining shape fidelity post-extrusion. The lower recovery in the composite ink could be attributed to the presence of CB particles, which may hinder the reformation of the network structure. Overall, both inks demonstrate suitable rheological properties for DIW printing applications.

4.2. DIW of graded filler concentration extrudates

The step function and gradient prints are successfully produced using the continuous mixing setup on the modified Ender 3 Pro DIW printer. A white plasticized starch ink and a red colored ink are used to visualize the transition zone in the prints. The results of these printed samples are shown in Figs. 6 and 7. Fig. 6a shows the color transition from the pure plasticized starch to a red colored plasticized starch ink with a step function. It is clear that multiple lines are still printed in the white color, after which some light red can be observed. The delay in the appearance of the red color is due to the dead volume inside the static mixer, which only contains white when the switch is made. At the moment of the transition, the red stream starts entering the mixing zone. At first some mixing with the remaining white ink in the mixer takes place. After some more lines, the color becomes fully red, indicating that the white ink has been completely flushed out of the mixer. The color change is analyzed using image color analysis to quantify the transition zone. Every 120 mm along the strand, the L^*, a^* and b^* values are determined and the difference with the color at the beginning of the extrusion is calculated using Eq. (1) and scaled such that the difference can be reported as a transition from white to red between 0 and 1 respectively. This is shown in Fig. 6b, which gives the scaled color difference ΔE^*_{Lab} along the printed strand for the extruded step function versus the extruded volume. The different stages of the process are indicated on the graph. It can be seen that after switching the extrusion from white to red, the color remains white for approximately 0.5 ml, indicated by a value of 0 on the graph. After this delay, the value of the color difference starts to increase, as the red ink starts to appear in the printed strand due to the flushing of the white ink from the mixer. Finally, after an additional 0.4 ml, the color difference reaches 1, indicating that the printed material is fully red. The total transition zone takes approximately 0.9 ml, which is around 4 times the theoretical dead volume. This can be explained by matrix material sticking to the baffles in the mixer and being flushed out more slowly than the bulk material.

When comparing the experimental data to the simulated curves, it can be seen that the simulation predicts a similar trend, with a delay in the color change due to the dead volume and a gradual transition from white to red. However, the simulated transition of both the maximum and the average dye concentration start earlier than the experimental one, indicating that the red ink is extruded slower than expected. It should be noted that the simulated influence of rheology on the outlet concentration dynamics was found to be minor under the present flow conditions. Despite variations in viscosity or shear rate dependent behavior, the overall shape of the concentration curves, the dead-zone duration and the characteristic volumes required to reach the steady state remain nearly unchanged, as demonstrated in **Figure S.9** in the SI. This indicates that the transport of the dye is primarily governed by advection and geometric mixing and there is no interaction with the rheology. Once the color change is observed in the experiments, the transition goes faster than the simulated one. The experimental color transition being complete after a smaller extruded volume than anticipated might be caused by the fact that a small amount of red dye in the ink is sufficient to reach the same color as for the final extrusion ratio. Moreover, preferential flowing paths can be present in the mixing nozzle, leading to a faster extrusion of the colored ink compared to the simulation where perfect mixing and flow is assumed. The concentration fields show full symmetry, which indicates that the three mixing elements are sufficient to achieve efficient mixing under the investigated operating conditions. However, the longer residence time close to the mixer walls causes a moderate radial concentration gradient during the transition. Increasing the number of mixing elements would therefore be expected to yield only marginal improvements and would increase the dead volume. Overall, the results demonstrate the capability of the continuous mixing setup to create a step change in composition during DIW printing, with a quantifiable transition zone.

In Fig. 7, the color transition from pure plasticized starch to red colored plasticized starch with gradient printing is shown. Here the extrusion ratio is gradually changed from 100% white to 100% red or 50% red over the length of the printed sample, starting after the second printed line. Two different gradient slopes are programmed in the G-code, a fast gradient, pictured in Fig. 7a and analyzed in Fig. 7b and a slow gradient, shown in Fig. 7c and analyzed in Fig. 7d. A smooth transition from white to red can be observed in both cases, indicating that the continuous mixing setup is able to create a gradient in composition during printing. These transitions are much more gradual compared to the step function print, demonstrating the tunability of the continuous mixing setup to print intermediate concentrations.

The pictures in Fig. 7 are analyzed using image color analysis to quantify the transition zones in both prints. In Fig. 7b, the scaled color difference ΔE^*_{Lab} along the printed sample with continuous gradient extrusion is plotted versus the extruder volume. The different stages of the process are indicated on the graph. Here, the color change also starts to be noticeable after approximately 0.5 ml of extrusion, which is similar to the dead volume observed in the step function print. After this point, the color difference increases gradually as the extrusion ratio is changed from white to red. For the fast gradient, the color difference reaches the value of 1 after a transition of approximately 0.8 ml, which is double the transition volume of the step function but less than the anticipated volume of 1.5 ml. This indicates that the continuous mixing setup is able to create a smooth gradient in composition during printing, with a transition zone that is larger than that of the step function print due to the gradual change in extrusion ratio. In red, the simulated transition of the maximal (full line) and average (dashed line) dye concentration of

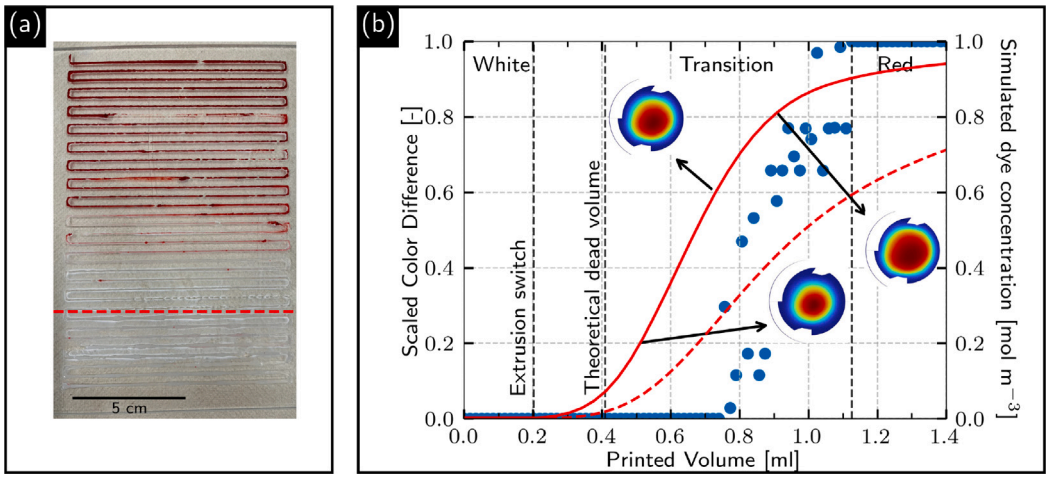

Fig. 6. Optical characterization and simulation of the printed step function. (a) Picture of the color transition from pure plasticized starch to red colored plasticized starch. The red dashed line indicates the position at which the extrusion switches from white to red. (b) Color transition from pure plasticized starch to colored plasticized starch with step function printing. The different stages of the process are indicated on the graph and the simulated maximal and average dye concentration are plotted as a full and dashed red line respectively. Cross section images of the simulated dye concentration at the outlet of the mixing channel at different time points during the step function extrusion are shown, hereby dark blue indicates 0 mol m^{-3} and dark red indicates 1 mol m^{-3}.

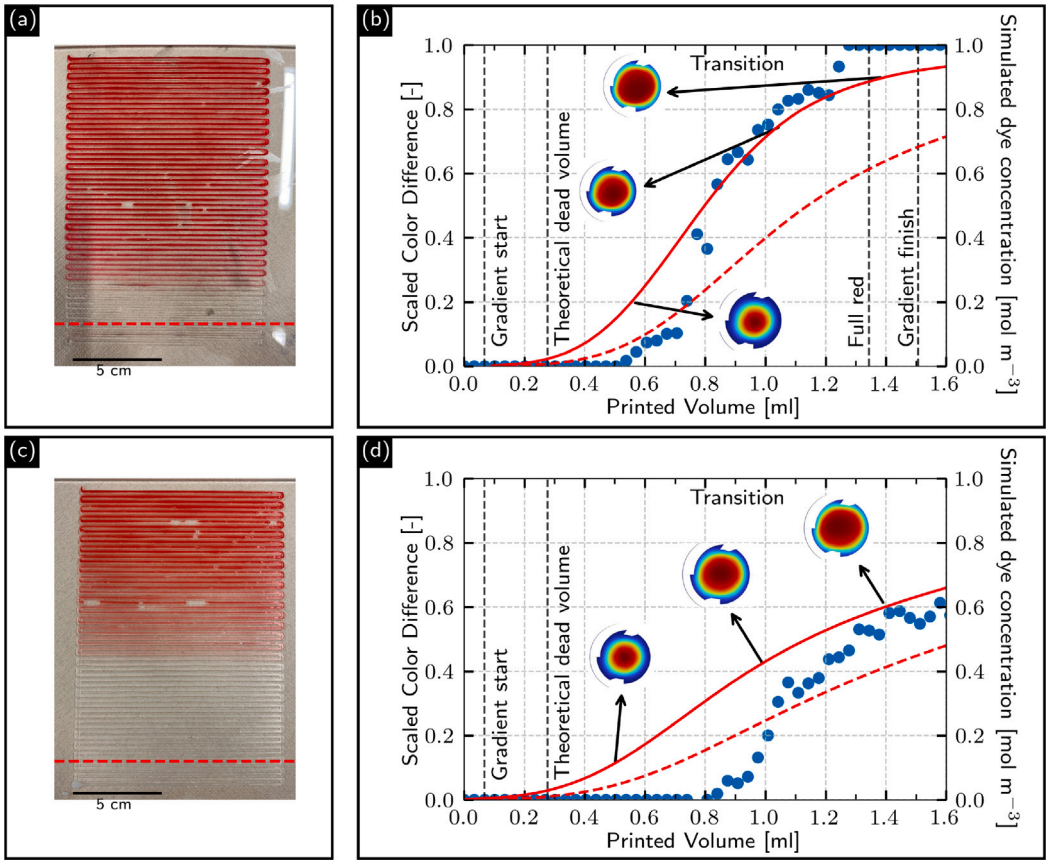

Fig. 7. Optical characterization and simulation of the printed gradient functions. Picture of the (a) fast and (c) slow color transition from pure plasticized starch to red colored plasticized starch. The red dashed lines indicate the position at which the extrusion switch starts. Color transition from pure plasticized starch to colored plasticized starch during the (b) fast and (d) slow gradient printing. The different stages of the process are indicated on the graph as well as the simulated maximal and average dye concentrations (red full and dashed lines respectively). Cross section images of the simulated dye concentration at the outlet of the mixing channel at different time points during the gradient function extrusions are shown, hereby dark blue indicated 0 mol m^{-3} and dark red indicates 1 mol m^{-3}.

this gradient are plotted. Here it can be observed that the onset of the color change agrees well with the profile of the average simulated dye concentration and the later part of the transition follows more the trend of the maximum simulated dye concentration. A similar conclusion as for the step function can thus be made. The experiments reach the total color change again slightly faster than the simulation predicts, which can be due to a full red color with a smaller amount of dye.

The transition zone of the gradient can be further optimized by altering the extrusion ratios during the print, for example by slowing down the change in extrusion rate to create a slower transition. A gradient at half the speed of the fast gradient is also printed and analyzed, as shown in Fig. 7d. Here, the red color appears after a delay of approximately 0.7 ml of extrusion, which is due to the dead volume of the mixer and the slower change in extrusion ratio. After extrusion of the same volume as for the fast gradient, the color difference only reaches a value of 0.6, indicating that the transition is indeed slower. This shows that the continuous mixing setup allows for control over the gradient slope by adjusting the rate of change in extrusion ratios during printing. When looking at the comparison between the experimental and simulated transitions (Figs. 6 and 7), it can be seen that the experimental data agree well with the simulated trends. Most of the data points of the experimental color difference are within the range of the simulated maximum and average dye concentration, which indicates that the simulations capture the main features of the mixing process. However, it can be observed that the onset delay of the experimental data increases when the programmed transition is slower. This effect is not captured in the simulations, which indicates deviations from pure advective transport. Therefore, experimental verification of the printed concentration profiles is essential in gradient printing.

At some locations in Figs. 6a, 7a and c, defects in the printed samples can be observed. These small zones without material deposition are most likely due to entrapped air in the syringes or the mixing nozzle. When loading these viscous inks into the syringes, air bubbles can be trapped inside, which can lead to interruptions in the extrusion during printing. Careful loading of the syringes and priming of the mixing nozzle can help to minimize these defects. Moreover, when starting a print, air can be entrapped inside the nozzle if both streams do not reach the junction point at the same time. It is important to ensure that the mixing nozzle is fully primed before starting the print, meaning that the ink which should be extruded first is already present at the outlet of the nozzle and the second one at the junction point.

Overall, the mixing setup demonstrates a promising capability to print objects with continuously varying parameters, such as color or filler content, by controlling the extrusion ratios of two different inks. This opens up possibilities for creating functionally graded materials with tailored properties for various applications. One intrinsic disadvantage of this type of mixing nozzle is the dead volume. This dead volume is a trade-off between the length of the static mixer and the total volume needed for a transition from one composition to another. More mixing elements lead to better mixing but also to a larger dead volume. Depending on the application, one can choose to optimize for better mixing or for a smaller dead volume (faster transitions). Moreover, the nozzle does not need to be primed with a pure ink composition, but can also be primed with an intermediate composition to reduce the dead volume effect. The dead volume is now around 10% of the total extrudable volume, being two 5 ml syringes. A scale-up towards larger syringes can also help to reduce the relative effect of the dead volume on the total printed object.

4.3. Determination of the percolation threshold

Two snake-like samples are printed in which the extrusion rates of both inks are varied per two lines to obtain a transition from pure plasticized starch to a composite ink with a high CB loading (~10 wt%). This protocol resembles the gradient strand discussed in Section 4.2 and shown with a color transition in Fig. 7a. The dried printed samples are characterized electrically by measuring the resistance at different points along the strand and thermogravimetrically by cutting small segments at different locations to determine the local CB loading. First, several samples of the pure plasticized starch matrix from both prints are analyzed via TGA to determine a residue baseline for the percolation threshold determination. These samples rendered and open loop measurement on the multimeter, indicating a resistance larger than 500 MΩ. This average residue is subtracted from the residue values of the composite samples from the respective prints to correct for any residue originating from the matrix itself. The gradual increase of CB loading along the printed samples is visualized in Fig. 8a where both prints are represented by a different symbol. It is important to note here that since concentrations are measured locally, the dead volume and delays in concentration changes as compared to the predicted values do not affect the determined EPT values. The simulations do indicate the need for such local concentration measurements, as the printed gradient is no exact copy of the programmed G-code sequence.

The theoretical printed composition is indicated by the green dashed line. The results of the conductivity measurements as a function of CB loading are shown as datapoints in Fig. 8b. The conductivity σ is calculated based on the measured resistance R, the length of the tested sample L_r and the estimated cross-sectional area A of the printed strand, which was 0.28 mm^2, as described in Eq. (2). The Boltzmann-sigmoidal function is fitted to all the data using non-linear least squares and is shown as the orange dashed line in Fig. 8. The fitting parameters in Eq. (4) are determined to be $A_1 = 9.3 \cdot 10^{-5}$ S m^{-1}, $A_2 = 16.6$ S m^{-1}, $A_3 = 1.0$ $wt\%^{-1}$ and $A_4 = 2.7$ wt%. These values represent the minimum and maximum average conductivity, the slope at the inflection point and the concentration at the inflection point respectively. The latter is also the EPT of the composite as it represents the concentration at which the largest increase in conductivity occurs. The standard error on the EPT based on the data in Fig. 8b is ±0.3 wt %. This error is mostly determined by the concentration data points in the transition region and taking more samples around this region would thus enhance the accuracy of the determined EPT. The jump in conductivity around the EPT can be found in A_3 and is 1 order of magnitude over a concentration range of 1 wt%. This is a less steep increase compared to literature values for similar systems, which can be due to the fine resolution in concentration obtained via the gradient printing method. The overall increase in conductivity from the lowest to the highest measured concentration is around five orders of magnitude, indicating a significant enhancement in electrical properties due to the addition of CB filler. The determined EPT is further in line with literature values for similar systems but can be determined much faster and with only one sample using this method [27,28]. It is also worth to mention again that variations in EPT can occur due to differences in processing methods, filler dispersion, and matrix properties. Since the dispersion quality was not optimized in the current work, it might be possible to reduce the EPT of this material and thus to shift the curve in Fig. 8b to the left.

5. Conclusion and outlook

In this work, a low-cost continuous mixing setup for direct ink writing additive manufacturing is developed. The setup is used to print plasticized starch-based composite inks with a gradient in carbon black filler content. The continuous mixing setup is successfully implemented on an Ender 3 Pro FDM printer, modified for DIW printing. This allows for the printing of gradient composition samples. The rheological characterization of both the pure plasticized starch ink and the composite ink shows that both materials exhibit suitable properties for DIW printing. The materials show a predominantly elastic behavior, shear thinning, and good structural recovery after shear. The addition of carbon black increases the stiffness and yield stress of the ink, but does not significantly alter its flow behavior. Optical characterization of the printed colored samples demonstrates the ability to create smooth transitions in composition. However, the transition zone is influenced

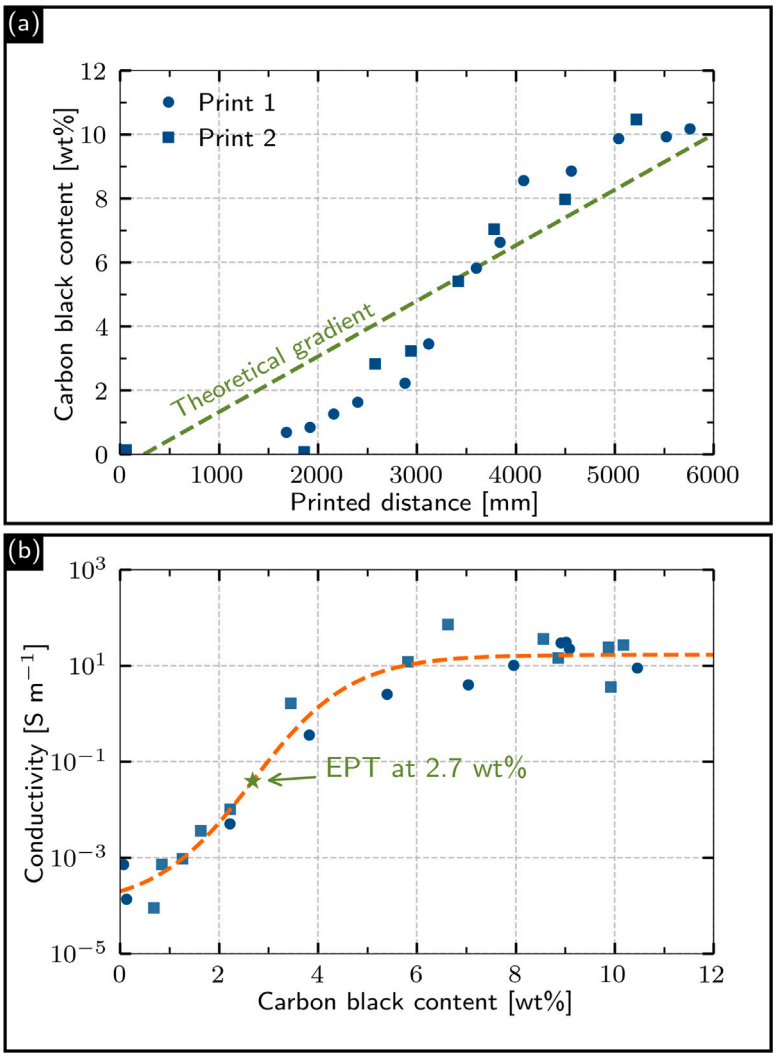

Fig. 8. (a) Carbon black loading along the printed samples. The green dashed line indicates the theoretical composition profile for two samples printed with a fast gradient. (b) Electrical conductivity of the plasticized starch-based composite ink as a function of carbon black content. The data is fitted with a sigmoidal function, as shown by the orange dashed line and the electrical percolation threshold is determined to be 2.7 wt% CB.

by the dead volume in the static mixer. Electrical characterization of segments of the printed gradient composition samples enables the determination of the electrical percolation threshold of the composites. By performing TGA on the same segments, this electrical percolation threshold is found to be 2.7 wt% carbon black loading. This method provides a fast and efficient way to determine the percolation threshold compared to traditional methods. Instead of producing different samples of different filler loadings and testing each one of them for electrical conductivity, only two different loadings are needed now, one below and one above percolation. Consequently, our approach saves time and material compared to the traditional sample by sample testing. However, printability of the materials is an extra requirement to use gradient additive manufacturing. The developed setup is suitable for a wide range of viscoelastic materials, as long as they can be extruded through the nozzle, have a suitable yield stress and do not cause clogging. The main limitation of the setup is expected to be the maximum viscosity that can be extruded, which is determined by the torque of the stepper motor and the geometry of the nozzle. Hereby, it should be kept in mind that the static mixer creates an extra pressure loss, which makes the rheological requirements more stringent for gradient printing than for standard DIW printing. In principle, mixing nozzles can be implemented for filament-based FDM printing as well, allowing to determine the EPT of thermoplastic composites. Thereto, the design of the mixing nozzle would need to be adapted to the higher temperatures and viscosities involved in FDM.

The developed continuous mixing setup opens up new possibilities for creating functionally graded materials with different material systems and gradient profiles for various applications like nutrient and color gradients in food printing, mechanical gradients in tissue engineering, or gradients in electrical and thermal properties in electrically and thermally functional materials. Further improvements to the hardware can be made to steer the trade-off between mixing quality and relative dead volume in the static mixer. The printing process can also be optimized to reduce defects in the printed strands, such as air entrapment.

CRediT authorship contribution statement

Stijn De Smedt: Writing – original draft, Visualization, Validation, Methodology, Investigation, Formal analysis, Data curation, Conceptualization. **Quanrun Dong:** Writing – review & editing, Validation, Software, Methodology, Formal analysis. **Francisco Molina-Lopez:** Writing – review & editing, Conceptualization. **Ruth Cardinaels:** Writing – review & editing, Supervision, Resources, Project administration, Methodology, Funding acquisition, Conceptualization.

Declaration of Generative AI and AI-assisted technologies in the writing process

During the preparation of this work the authors used Microsoft Copilot to help with the data processing and review the language. Moreover, ChatGPT was also used to help with language refinement and clarity. After using these tools, the authors reviewed and edited the content as needed and take full responsibility for the content of the published article.

Declaration of competing interest

The authors declare the following financial interests/personal relationships which may be considered as potential competing interests: Ruth Cardinaels reports financial support was provided by European Union. Quanrun Dong reports financial support was provided by China Scholarship Council. If there are other authors, they declare that they have no known competing financial interests or personal relationships that could have appeared to influence the work reported in this paper.

Acknowledgments

The authors acknowledge the financial support from the European Research Council (ERC) under the European Union's Horizon 2020 research and innovation programme (Grant agreement No. 948739 - PEM-Sprint). Q. Dong acknowledges the China Scholarship Council for a PhD fellowship. The authors gratefully acknowledge J. De Ceulaer for performing TGA measurements and F. Ghys for optimizing the plasticized starch composition.

Appendix A. Supplementary data

Supplementary material related to this article can be found online at https://doi.org/10.1016/j.coco.2026.102850.

Data availability

Data will be made available on request.

References

[1] A.S. Alshammari, 14 - carbon-based polymer nanocomposites for sensing applications, in: A.F. Ismail, P.S. Goh (Eds.), Carbon-Based Polymer Nanocomposites for Environmental and Energy Applications, Elsevier, 2018, pp. 331–360, http://dx.doi.org/10.1016/B978-0-12-813574-7.00014-9.

[2] S. Shaji, A. Anna, K. S., A. Aboobaker, Review on sustainable flexible electronics: exploring the potential of chitosan, cellulose starch, silk fibroin and gelatin, Discov. Polym. 2 (2025) 19, http://dx.doi.org/10.1007/s44347-025-00031-7.

[3] H.A. Bashid, H.N. Lim, S.M. Hafiz, Y. Andou, M. Altarawneh, Z.T. Jiang, N.M. Huang, 16 - modification of carbon-based electroactive materials for supercapacitor applications, in: A.F. Ismail, P.S. Goh (Eds.), Carbon-Based Polymer Nanocomposites for Environmental and Energy Applications, Elsevier, 2018, pp. 393–413, http://dx.doi.org/10.1016/B978-0-12-813574-7.00016-2.

[4] H.-J. Choi, M.S. Kim, D. Ahn, S.Y. Yeo, S. Lee, Electrical percolation threshold of carbon black in a polymer matrix and its application to antistatic fibre, Sci. Rep. 9 (2019) 6338, http://dx.doi.org/10.1038/s41598-019-42495-1.

[5] Y. Wang, J. Huang, G. Zhao, R. Chen, J. Huang, X. Chang, J. Li, Y. Zhu, Flexible conductive hydrogels through optimized interfacial connectivity of hybrid fillers toward efficient electromagnetic interference shielding and wearable strain sensors, Compos. Commun. 60 (2025) 102611, http://dx.doi.org/10.1016/j.coco.2025.102611.

[6] N. Qureshi, V. Dhand, S. Subhani, R.S. Kumar, N. Raghavan, S. Kim, J. Doh, Exploring conductive filler-embedded polymer nanocomposite for electrical percolation via electromagnetic shielding-based additive manufacturing, Adv. Mater. Technol. 9 (2024) 2400250, http://dx.doi.org/10.1002/admt.202400250.

[7] Z.A. Karim, A. Hafeez, A.F. Ismail, 1 - the fabrication of carbon-based polymer nanocomposite, in: A.F. Ismail, P.S. Goh (Eds.), Carbon-Based Polymer Nanocomposites for Environmental and Energy Applications, Elsevier, 2018, pp. 3–25, http://dx.doi.org/10.1016/B978-0-12-813574-7.00001-0.

[8] Y. Huang, W. Wang, X. Zeng, X. Guo, Y. Zhang, P. Liu, Y. Ma, Y. Zhang, Effects of the filler size on the electrical percolation threshold of carbon black–carbon nanotube–polymer composites, J. Appl. Polym. Sci. 135 (2018) 46517, http://dx.doi.org/10.1002/app.46517.

[9] R. Arjmandi, A. Hassan, N. Othman, Z. Mohamad, 3 - characterizations of carbon-based polypropylene nanocomposites, in: A.F. Ismail, P.S. Goh (Eds.), Carbon-Based Polymer Nanocomposites for Environmental and Energy Applications, Elsevier, 2018, pp. 57–78, http://dx.doi.org/10.1016/B978-0-12-813574-7.00003-4.

[10] A. Kaidarova, V. Naenen, R. Windey, N. Goossens, T. Sinha, V. Ignatious, B. Zhang, T.P. Mach, M. Wevers, J. Vleugels, F. Molina-Lopez, Hybrid organic–inorganic functional nanocomposites: From basis to applications in stretchable sensing and energy devices, Mater. Sci. Eng. R 163 (2025) 100933, http://dx.doi.org/10.1016/j.mser.2025.100933.

[11] M. Xu, Y. Liu, Z. Wang, Z. Ying, W. Yu, L. Zhu, D. Hu, L. Zhang, L. Zhao, Engineered polyamide 66-based composites towards superior electrical conductivity and enhanced toughness, Compos. Commun. 60 (2025) 102616, http://dx.doi.org/10.1016/j.coco.2025.102616.

[12] J. Payandehpeyman, M. Mazaheri, Micromechanical modeling of electrical conductivity and percolation in cnt/polymer nanocomposites by considering morphology: Homogeneous, agglomerated, and segregated structures, Polym. Compos. 45 (2025) 16240–16259, http://dx.doi.org/10.1002/pc.70042.

[13] H. Ahmadi, H. Nazockdast, Z. Ahmadi, P.D. Anderson, R. Cardinaels, Tuning the carbon nanotube conductive network in pla-based immiscible blends via stereocomplex crystallization, Composites Part B 308 (2026) 112973, http://dx.doi.org/10.1016/j.compositesb.2025.112973.

[14] A. Bharati, R. Cardinaels, J.W. Seo, M. Wübbenhorst, P. Moldenaers, Enhancing the conductivity of carbon nanotube filled blends by tuning their phase separated morphology with a copolymer, Polymer 79 (2015) 271–282, http://dx.doi.org/10.1016/j.polymer.2015.09.080.

[15] Z. Gao, M. Li, Y. Li, H. Cheng, C. Liu, C. Shen, A multi-scale interface-induced magnetic–dielectric synergy in polymeric heterostructures for superior electromagnetic wave absorption, Compos. Commun. 60 (2025) 102657, http://dx.doi.org/10.1016/j.coco.2025.102657.

[16] L. Ye, J. Hong, Z. Zhang, G. Wu, Y. Li, Optimizing thermal and electrical transport pathways in polymercomposites via in-situ graphite exfoliation, Compos. Commun. 54 (2025) 102276, http://dx.doi.org/10.1016/j.coco.2025.102273.

[17] S. Kale, F.A. Sabet, I. Jasiuk, M. Ostoja-Starzewski, Effect of filler alignment on percolation in polymer nanocomposites using tunneling-percolation model, J. Appl. Phys. 120 (2016) 045105, http://dx.doi.org/10.1063/1.4959610.

[18] M. Safdari, M.S. Al-Haik, 5 - a review on polymeric nanocomposites: Effect of hybridization and synergy on electrical properties, in: A.F. Ismail, P.S. Goh (Eds.), Carbon-Based Polymer Nanocomposites for Environmental and Energy Applications, Elsevier, 2018, pp. 113–146, http://dx.doi.org/10.1016/B978-0-12-813574-7.00005-8.

[19] A. Sharma, 8 - alignment of carbon nanotubes in polymer matrix, in: A.F. Ismail, P.S. Goh (Eds.), Carbon-Based Polymer Nanocomposites for Environmental and Energy Applications, Elsevier, 2018, pp. 199–214, http://dx.doi.org/10.1016/B978-0-12-813574-7.00008-3.

[20] J. Kim, S.G. Song, N.-H. You, S.G. Kim, B.-C. Ku, Enhanced electrical and thermal properties of expanded graphite-polyphenylene sulfide (PPS) composites through in-situ polymerization for fuel cell bipolar plates, Compos. Commun. 53 (2025) 102252, http://dx.doi.org/10.1016/j.coco.2025.102252.

[21] H. Du, C. Gao, X. Xia, G. Weng, Field-tuned CNT alignment and frequency dependence of electrical properties of CNT based nanocomposites, Appl. Math. Model. 156 (2026) 116768, http://dx.doi.org/10.1016/j.apm.2026.116768.

[22] H. Du, C. Fang, J. Zhang, X. Xia, G. Weng, Segregated carbon nanotube networks in CNT-polymer nanocomposites for higher electrical conductivity and dielectric permittivity, and lower percolation threshold, Internat. J. Engrg. Sci. 173 (2022) 103650, http://dx.doi.org/10.1016/j.ijengsci.2022.103650.

[23] X. Lu, L. Pichon, J. Bai, Multiscale modeling and numerical analyses of the electric conductivity of CNT/polymer nanocomposites taking into account the tunneling effect, Int. J. Numer. Model. 34 (2021) e2955, http://dx.doi.org/10.1002/jnm.2955.

[24] S. Azizi, E. David, M.F. Fréchette, P. Nguyen-Tri, C.M. Ouellet-Plamondon, Electrical and thermal phenomena in low-density polyethylene/carbon black composites near the percolation threshold, J. Appl. Polym. Sci. 136 (2019) 47043, http://dx.doi.org/10.1002/app.47043.

[25] M.P. da SiIva, S.N. Cavalcanti, A.M. Alves, D.M.G. Freitas, P. Agrawal, E.O. Vilar, T.J.A. de Mélo, Evaluation of the rheological and electrical percolation of high-density polyethylene/carbon black composites using mathematical models, Polym. Eng. Sci. 61 (2021) 2105–2116, http://dx.doi.org/10.1002/pen.25738.

[26] J. Ma, J. Zhu, S. Zhou, C. Zhao, C. Liu, Z. Xin, J. Cai, J. He, P. Feng, L. Guo, X. Tao, Multifunctional starch-based conductive hydrogels for smart sensors and flexible supercapacitors, Int. J. Biiol. Macromol. 302 (2025) 140430, http://dx.doi.org/10.1016/j.ijbiomac.2025.140430.

[27] X. Ma, P.R. Chang, J. Yu, P. Lu, Characterizations of glycerol plasticized-starch (gps)/carbon black (cb) membranes prepared by melt extrusion and microwave radiation, Carbohydr. Polymers 74 (2008) 895–900, http://dx.doi.org/10.1016/j.carbpol.2008.05.015.

[28] H. Peidayesh, K. Mosnáčková, Z. Špitalský, A. Heydari, A.O. Šišková, I. Chodák, Thermoplastic starch–based composite reinforced by conductive filler networks: Physical properties and electrical conductivity changes during cyclic deformation, Polymers 13 (2021) http://dx.doi.org/10.3390/polym13213819.

[29] S.K. Parupelli, S. Desai, Hybrid additive manufacturing (3d printing) and characterization of functionally gradient materials via in situ laser curing, Int. J. Adv. Manuf. Technol. 110 (1–2) (2020) 543–556.

[30] H. Wu, W. Fahy, S. Kim, H. Kim, N. Zhao, L. Pilato, A. Kafi, S. Bateman, J. Koo, Recent developments in polymers/polymer nanocomposites for additive manufacturing, Prog. Mater. Sci. 111 (2020) 100638, http://dx.doi.org/10.1016/j.pmatsci.2020.100638.

[31] M.J. Fasolka, C.M. Stafford, K.L. Beers, Gradient and microfluidic library approaches to polymer interfaces, in: M. Meier, D. Webster (Eds.), Polymer Libraries. Advances in Polymer Science, Springer, Berlin, Heidelberg, 2010, pp. 63–105, http://dx.doi.org/10.1007/12_2009_17.

[32] M. Sahaluddin, M. Abdulhafez, S. Ghosh, M. Bedewy, Spatially varying wettability and resistivity in laser-induced graphene for flexible microfluidics, programmable heaters, and thermochromic displays, Carbon 250 (2026) 121304, http://dx.doi.org/10.1016/j.carbon.2026.121304.

[33] C. Zhu, P. Liu, J. Chen, Z. Ding, G. Tang, Q. Gao, Y. Ni, K. Xu, Z. Hao, G. Xu, F. Liu, Constructing ti3c2tx–mxene-based gradient woodpile structure by direct ink writing 3d printing for efficient microwave absorption, Int. J. Miner. Metall. Mater. 32 (2025) 657–667.

[34] H. Qu, C. Gao, K. Liu, H. Fu, Z. Liu, P.H.J. Kouwer, Z. Han, C. Ruan, Gradient matters via filament diameter-adjustable 3d printing, Nat. Commun. 15 (2024) 2930.

[35] D. Tang, L. Hao, Y. Li, Z. Li, Effect of clay functionally graded materials on dual gradient direct ink writing behavior and microstructure of geological model, Rapid Prototyp. J. 26 (2020) 39–48.

[36] Z. Cai, J. Zhang, L. Zhang, J. Wang, H. Chen, Y. Lv, X. Zhang, Fluid-assisted fused deposition modeling 3D printing of anisotropically thermally conductive polymer composites with precisely tunable heat transfer pathways, Compos. Commun. 46 (2024) 101835, http://dx.doi.org/10.1016/j.coco.2024.101835.

[37] C. Li, L. Ouyang, J.P. Armstrong, M.M. Stevens, Advances in the fabrication of biomaterials for gradient tissue engineering, Trends Biotechnol. 39 (2) (2021) 150–164, http://dx.doi.org/10.1016/j.tibtech.2020.06.005.

[38] B. Mirani, E. Stefanek, B. Godau, S.M.H. Dabiri, M. Akbari, Microfluidic 3D printing of a photo-cross-linkable bioink using insights from computational modeling, ACS Biomater. Sci. Eng. 7 (7) (2021) 3269–3280, http://dx.doi.org/10.1021/acsbiomaterials.1c00084.

[39] L. Serex, A. Bertsch, P. Renaud, Microfluidics: A new layer of control for extrusion-based 3D printing, Micromachines 9 (2) (2018) 86, http://dx.doi.org/10.3390/mi9020086.

[40] F. Feng, J. He, J. Li, M. Mao, D. Li, Multicomponent bioprinting of heterogeneous hydrogel constructs based on microfluidic printheads, Int. J. Bioprinting 5 (2) (2019) 202, http://dx.doi.org/10.18063/ijb.v5i2.202.

[41] W. Liu, Y.S. Zhang, M.A. Heinrich, F. De Ferrari, H.L. Jang, S.M. Bakht, M.M. Alvarez, J. Yang, Y.-C. Li, G. Trujillo de Santiago, et al., Rapid continuous multimaterial extrusion bioprinting, Adv. Mater. 29 (3) (2017) 1604630, http://dx.doi.org/10.1002/adma.201604630.

[42] A. Lavrentieva, T. Fleischhammer, A. Enders, H. Pirmahboub, J. Bahnemann, I. Pepelanova, Fabrication of stiffness gradients of GelMA hydrogels using a 3D printed micromixer, Macromol. Biosci. 20 (10) (2020) 2000107, http://dx.doi.org/10.1002/mabi.202000107.

[43] A. Krige, J. Haluška, U. Rova, P. Christakopoulos, Design and implementation of a low cost bio-printer modification, allowing for switching between plastic and gel extrusion, HardwareX 9 (2021) e00186, http://dx.doi.org/10.1016/j.ohx.2021.e00186.

[44] K. Pusch, T.J. Hinton, A.W. Feinberg, Large volume syringe pump extruder for desktop 3d printers, HardwareX 3 (2018) 49–61, http://dx.doi.org/10.1016/j.ohx.2018.02.001.

[45] N. Bunkluarb, W. Sawangtong, N. Khajohnsaksumeth, B. Wiwatanapataphee, Numerical simulation of granular mixing in static mixers with different geometries, Adv. Difference Equ. 238 (2019) http://dx.doi.org/10.1186/s13662-019-2174-5.

[46] R. Kumar, Thermal, pasting and morphological properties of starch granules of wheat (triticum aestivum l.) varieties, J. Food Sci. Technol. 54 (2017) 2403–2410, http://dx.doi.org/10.1007/s13197-017-2681-x.

[47] S. De Smedt, B. Attaianese, R. Cardinaels, Direct ink writing of particle-based multiphase materials: From rheology to functionality, Curr. Opin. Colloid Interface Sci. 75 (2025) 101889, http://dx.doi.org/10.1016/j.cocis.2024.101889.

[48] W. Mokrzycki, M. Tatol, Color difference delta e - a survey, Mach. Graph. Vis. 20 (2011) 383–411.

[49] A. Merzouki, N. Haddaoui, Electrical conductivity modeling of polypropylene composites filled with carbon black and acetylene black, Int. Sch. Res. Not. 2012 (2012) 493065, http://dx.doi.org/10.5402/2012/493065.

[50] M. Rahaman, A. Aldalbahi, P. Govindasami, P. Khanam, S. Bhandari, P. Feng, T. Altalhi, A new insight in determining the percolation threshold of electrical conductivity for extrinsically conducting polymer composites through different sigmoidal models, Polymers 9 (2017) 527, http://dx.doi.org/10.3390/polym9100527.

[51] P. Virtanen, R. Gommers, T.E. Oliphant, M. Haberland, T. Reddy, D. Cournapeau, E. Burovski, P. Peterson, W. Weckesser, J. Bright, S.J. van der Walt, M. Brett, J. Wilson, K.J. Millman, N. Mayorov, A.R.J. Nelson, E. Jones, R. Kern, E. Larson, C. Carey, I. Polat, Y. Feng, E.W. Moore, J. VanderPlas, D. Laxalde, J. Perktold, R. Cimrman, I. Henriksen, E.A. Quintero, C.R. Harris, A.M. Archibald, A.H. Ribeiro, F. Pedregosa, P.a..C. van Mulbregt, Scipy 1.0: fundamental algorithms for scientific computing in python, Nature Methods 17 (2020) 261–272, http://dx.doi.org/10.1038/s41592-019-0686-2.

[52] F.P. Incropera, D.P. DeWitt, Fundamentals of Heat and Mass Transfer, fifth ed., John Wiley & Sons, 2002.

[53] M. Regner, K. Ostergren, C. Tragardh, Influence of viscosity ratio on the mixing process in a static mixer: Numerical study, Ind. Eng. Chem. Res. 47 (2002) 3030–3036, http://dx.doi.org/10.1021/ie0708071.